Additive Manufacturing Letters 1 (2021) 100011

Contents lists available at ScienceDirect

Additive Manufacturing Letters

journal homepage: www.elsevier.com/locate/addlet

Revealing the true partitioning character of zirconium in additively manufactured polycrystalline superalloys

Arthur Després[a,*], Stoichko Antonov[b], Charlotte Mayer[c], Muriel Veron[a], Edgar F. Rauch[a], Catherine Tassin[a], Jean-Jacques Blandin[a], Paraskevas Kontis[b,d], Guilhem Martin[a]

[a] Univ. Grenoble Alpes, CNRS, Grenoble INP, SIMaP, F-38000 Grenoble, France
[b] Max-Planck-Institut für Eisenforschung GmbH, Max-Planck-Strasse 1, Düsseldorf 40237, Germany
[c] Aubert et Duval, Usine des Ancizes, Rue des villas, BP1, Les Ancizes 63770, France
[d] Department of Materials Science and Engineering, NTNU Norwegian University of Science and Technology, Trondheim 7034, Norway

ARTICLE INFO

Keywords:
Additive manufacturing
Nickel-based superalloys
Phase transformation
TEM
APT

ABSTRACT

Minor addition of zirconium is common in polycrystalline nickel-based superalloys, where it is believed that it segregates at grain boundaries and contributes to increase the creep resistance. However, in superalloys produced by additive manufacturing, zirconium may become detrimental as it promotes hot-cracking during the fabrication stage. Here, we clarify the controversial role of this element by studying its distribution at near atomic scale in the as-built and heat-treated microstructures. In the as-built microstructure, zirconium is almost exclusively found at grain boundaries. However, after heat-treatment, zirconium is no longer found at grain boundaries. Instead, it partitions in γ' precipitates and zirconium oxides particles. The formation of zirconia is shown to originate from the reduction of nano-particles of alumina by zirconium during heat-treatment. The absence of zirconium at grain boundaries in this state challenges the classic view often reported in the literature for superalloys.

1. Introduction

Zirconium has been identified as a detrimental addition element in polycrystalline nickel-based superalloys processed by powder-bed fusion additive manufacturing, see e.g. [1,2]. When the melt pool solidifies, zirconium partitions to the liquid, which lowers the solidus temperature and promotes the formation of hot-cracks at high angle grain boundaries (HAGBs) [1–3]. Thermodynamic simulations of solidification suggest that the concentration of zirconium in the liquid at the end of solidification exceeds that in the nominal composition by several orders of magnitude [2,4]. These predictions have been confirmed by atom probe tomography (APT) measurements showing elevated zirconium concentration at HAGBs in the as-built microstructure [1,2], i.e. at the location where solidification ends.

As a result, there have been several attempts to fabricate nickel-based superalloys without zirconium [2,5,6], all leading to a reduced hot-cracking sensitivity. Interestingly, in the work of Tang et al. [6], crack free nickel-based superalloys with acceptable tensile and creep properties have been obtained without zirconium addition. This might be surprising given that zirconium is traditionally considered as a key element to improve the creep resistance of superalloys. According to several textbooks [7,8], after heat-treatment (prior to creep) diffusion should enhance grain boundary segregation of zirconium, thus leading to an improved creep resistance. Despite these theoretical considerations, the literature gives no evidence of zirconium grain boundary segregation in heat-treated microstructures after traditional fabrication. By contrast, it is not excluded that, during heat-treatment, zirconium may partition to intermetallic particles (see e.g. study of Murata et al. [9] showing several zirconium compounds in a conventional superalloy).

In order to clarify the partitioning character of zirconium in nickel-based superalloys processed by laser powder bed fusion (L-PBF), we carried out a systematic investigation of its distribution at near-atomic scale in the as-built and post-heat-treated microstructure. Potential grain boundary segregation of zirconium was investigated by APT, while the formation of zirconium-rich particles was investigated by transmission electron microscopy (TEM).

2. Materials and methods

2.1. Processing

A powder batch of the γ'-hardened AD730® alloy was supplied by Aubert et Duval (composition in Table 1). Carbon, nitrogen and oxygen were measured by thermal conductivity-infrared absorption, while the

* Corresponding author.
E-mail address: arthur.despres@grenoble-inp.fr (A. Després).

https://doi.org/10.1016/j.addlet.2021.100011
Received 20 September 2021; Received in revised form 11 October 2021; Accepted 12 October 2021

Table 1
composition of the powder used for this study atomic percent (at.%), as measured by thermal conductivity-infrared absorption and inductively coupled plasma.

Ni	Cr	Co	Mo	W	Al	Ti	Nb	C	B	Fe	Zr	N	O
bal.	17.57	8.27	1.80	0.84	5.07	3.74	0.67	0.10	0.05	4.23	0.028	0.018	0.042

other elements were measured by atomic emission spectroscopy using inductively coupled plasma. The oxygen content in the initial powder, found to be 420 at. ppm (equal to 118 wt. ppm), is typical of powders used in additive manufacturing [10,11]. Note that it is, by contrast, well above those measured in cast and wrought products, which are usually about 10–30 at. ppm (or 3–10 wt. ppm) [12,13].

Samples of 70 mm in length × 13 mm in width × 10 mm in height (along the build direction) were built by L-PBF on a EOS M290 machine. The linear energy density, defined as laser power divided by scan speed, was set to 0.38 J/mm, this value being in the upper range of that used in previous studies (0.14 J/mm for Hariharan et al. [1], 0.04 J/mm–0.50 J/mm for Carter et al. [7]). The hatch spacing was 100 µm, and the laser scan direction was rotated by 67° between each deposited layer. The samples were built under argon atmosphere. After fabrication, the oxygen content was measured to be 350 at. ppm (100 wt. ppm). The decrease of the oxygen level after fabrication by laser powder bed fusion under inert atmosphere is consistent with the observations from Haines et al. [14]. We have shown in previous works [4,15] that these samples are sensitive to hot-cracking. After L-PBF fabrication, a sub-solvus solutionizing heat-treatment at 1080 °C for 4 h was applied, followed by ageing at 760 °C for 16 h. All heat-treatments were performed in air. Given the high-corrosion resistance of nickel-based superalloys, it is not expected that significant oxygen uptake should occur in the bulk of the sample during the heat-treatment.

2.2. Transmission electron microscopy

TEM observations were carried out to detect potential zirconium-rich particles. Thin foils were prepared from the as-built and the heat-treated microstructures, and observed in a FEG JEOL 2100F operating at 200 kV. Imaging was carried out in scanning transmission electron microscopy (STEM) mode. The local chemistry was investigated by maps of energy dispersive X-ray spectroscopy (EDX), using a SDD (Silicon Drift Detector) Centurio detector. The K_α emission ray was used for detecting all elements. Note that boron was not measured because of the detector limitation, nor carbon, because of surface contamination.

Carbon replicas, in which second-phase particles are placed on an amorphous carbon film after dissolution of the γ matrix [4], were also prepared and characterized. The chemistry of the particles was investigated by EDX-maps. Note that due to contamination from the sample preparation, oxygen cannot reliably be detected on carbon replicas. On the same region of interest, crystallographic phase recognition was also carried out using the Automated Crystallographic Orientation Mapping (ACOM) method. The principle of this technique is to acquire a map of nano quasi-parallel beam diffraction patterns, and to perform phase and orientation recognition at each position by comparing the diffraction patterns to simulated patterns of candidate phases and orientations [16]. A correlation index sensitive to the Bragg spots intensity is calculated between each acquired patterns and the set of simulated patterns in order to determine, in an automated way, the best solution. The reliability of a phase indexing is evaluated by the parameter $R = 100 \times (1 - I_1/I_2)$, where I_1 and I_2 are the correlation indices of the two best solutions. Having $R > 15$ is considered sufficient to ascertain that the identified phase is by far the best solution out of all candidates [16]. The list of candidate phases, in Table 2, contains all the phases identified in a preliminary work on the as-built microstructure of the same alloy [4], as well as other zirconium-rich phases.

Table 2
List of candidate crystallographic phases for identification of second-phase particles by ACOM. The γ' phase lattice parameters were established by X-ray diffraction.

Phase	Space group	a, b, c (A)	α, β, γ (°)	Ref.
γ'	$Pm\bar{3}m$ (221)	3.59, -, -	90, -, -	–
(Ti,Nb)(C,N)	$Fm\bar{3}m$ (225)	4,36, -, -	90, -, -	[17]
$(Cr,Mo)_3B_2$	P4/mbm (127)	5.79, -, 3.06	90, -, -	[18]
$(Cr,Mo)_5B_3$	I4/mcm (140)	5.88, -, 10.10	90, -, -	[18]
Ni_7Zr_2	C2/m(12)	4.82, 8.22, 11.13	90, 96.7, 90	[17]
(m) Al_2O_3	C2/m(12)	11.79, 2.91, 5.62	90, 103.7, 90	[19]
(t) Al_2O_3	$P\bar{4}m2$ (115)	5.59, -, 23.65	90, -, -	[20]
ZrC	$Fm\bar{3}m$ (225)	4.68, -, -	90, -, -	[21]
(c) ZrO_2	$Fm\bar{3}m$ (225)	5,09, -, -	90, -, -	[22]
(t) ZrO_2	$P4_2/nmc$ (137)	3.60, -, 5.18	90, -, -	[23]
(m) ZrO_2	$P2_1/c$	5.15, 5.21, 5.32	90, 99.2, 90	[23]

2.3. Atom probe tomography

APT analysis was carried out in the as-built and heat-treated microstructures to measure grain boundary segregation. First, in the as-built and heat-treated microstructures, grain boundaries with specific misorientation angles were identified by electron backscattered diffraction (EBSD). Then, specimens were prepared using a FEI Dual Beam FIB Helios 600i. Site specific lift-outs were prepared following the procedure described in [24] to ensure that the grain boundaries are included in the specimen. A FIB image is shown in supplementary material (Fig. S1) to illustrate the method. Finally, the APT specimens were analysed using a Cameca LEAP 5000 XR instrument operating in a laser mode with pulse rate at 125 kHz, pulse energy 45–60 pJ and temperature 60 K. The commercial package AP Suite 6.1 was used for data reconstruction and analyses.

3. Results

3.1. Zirconium-rich particles in the as-built and heat-treated microstructures

Fig. 1 shows the STEM and X-ray count maps measured on a thin foil prepared from the as-built microstructure. In agreement with previous observations [2,25–27], the microstructure is composed of solidification cells (revealed by titanium segregations in the intercellular regions) and many particles located mostly in the intercellular regions. Alumina particles are detected without ambiguity thanks to their strong aluminium and oxygen signal. The presence of alumina, i.e. aluminium oxides, can be regarded as a specific feature of parts made by powder based additive manufacturing, as it is a direct consequence of their high oxygen content compared their cast or wrought counterparts. Numerous titanium and niobium-rich particles, as well as a few chromium-rich particles can also be detected. Note that as the matrix already contains about 17 at.% of chromium (Table 1), the contrast is rather weak with the chromium-rich particles. Fig. 1 is representative of several maps taken at the same magnification. No zirconium-rich particles were found.

Fig. 2 shows the phase identification performed on the carbon replica prepared from the as-built microstructure. The dark regions correspond to the amorphous carbon film. In Fig. 2a, the X-ray count maps show particles containing either aluminium, titanium or chromium, which

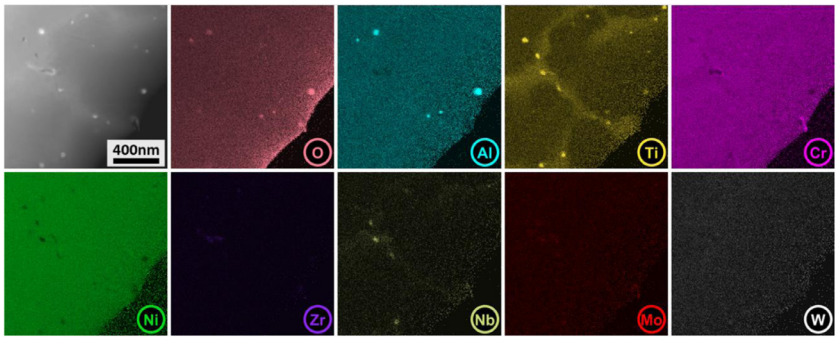

Fig. 1. STEM annular dark-field image and X-ray count maps measured by EDX on a thin foil prepared from the as-built microstructure. The colour contrast is proportional to the number of X-rays counted for each element.

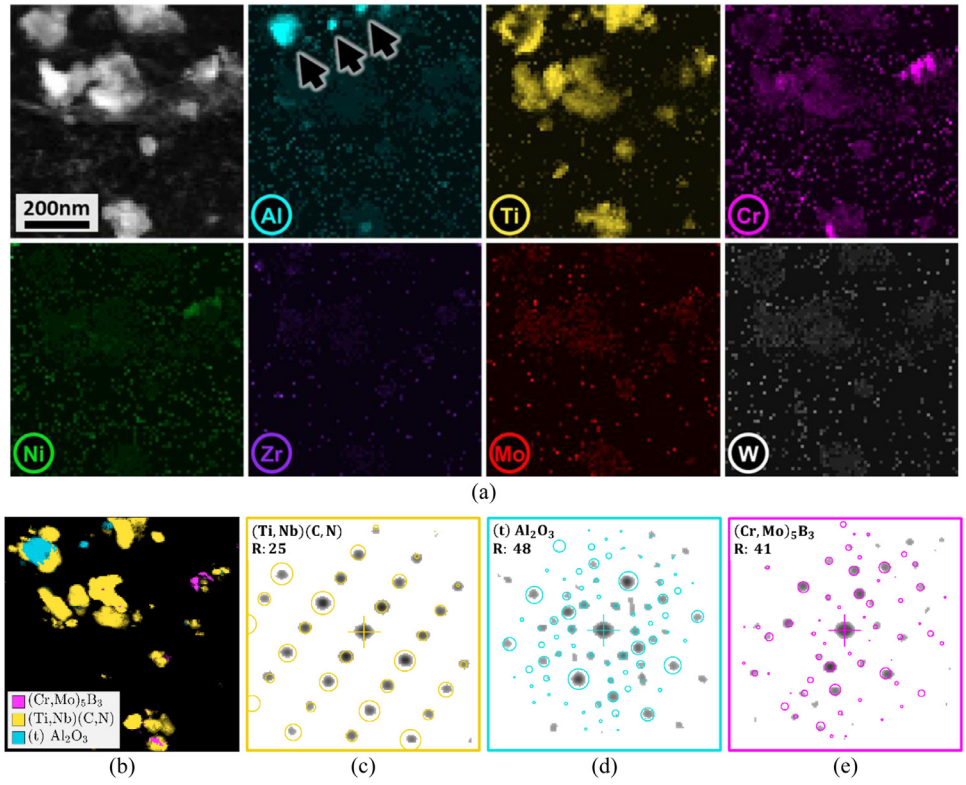

Fig. 2. Observation of a carbon replica prepared from the as-built microstructure. (a) STEM annular dark-field image and X-ray count maps measured by EDX. The colour contrast is proportional to the number of X-rays counted for each element. (b) crystallographic phase map obtained by ACOM on the same region of interest. (c–e) examples of acquired diffraction patterns (spots) with the corresponding simulated diffraction patterns (circles).

is consistent with the observations shown in Fig. 1. Fig. 2b indicates that their crystallographic phases are tetragonal (t) alumina, titanium-niobium carbonitride and chromium boride, respectively. The term carbonitride here is generic, and includes carbides, nitrides and carbonitrides, as it was previously shown that the full spectrum of composition can be found in this microstructure [4]. Fig. 2c to e show that the diffraction patterns of the three phases are well indexed. The phase reliability R overlaid on the pattern is for all cases well above 15, and except for a few small and faint spots (indicating diffraction far from the exact Bragg conditions), the simulated diffraction patterns (in circles) match very well with the acquired diffraction patterns (in spots). The success of the phase identification is further confirmed by the good correspondence between the chemistry of the particles and the chemistry expected from the recognized crystallographic phases.

In Fig. 2a and b, some carbonitrides are found attached to the alumina particles. This feature has already been noticed in several works [4,11,14], and has been related to the formation sequence of the different phases. Alumina likely forms at very high temperature prior to the γ matrix phase [4,14] or is already there in the powder feedstock, while carbonitrides form near the end of solidification. The alumina particles may then act as nucleation sites for carbonitrides.

Fig. 3 shows the observation conducted on a thin foil of the post-heat-treated microstructure. The γ' precipitates are easily distinguished due to their large volume fraction, their morphology, and their aluminium, titanium and nickel enrichments. Both primary γ' (~micron sized, formed during solutionizing) and secondary γ' (~50 nm sized, likely nucleated during cooling from solutionizing and grown during ageing) are observed. A few particles in the top right and bottom left corners present much stronger titanium enrichment. Finally, particles presenting strong zirconium and oxygen peaks suggest that zirconia (i.e. zirconium oxides) have formed during heat-treatments. By contrast with the as-built microstructure, and after examination of several maps of the same area, no alumina particles seem to be present in the heat-treated microstructure.

Fig. 4 shows observations conducted on a carbon replica prepared from the heat-treated sample. Fig. 4a shows a large number of γ' precipitates. A few particles are associated with isolated peaks of titanium, and others associated with zirconium. In Fig. 4b, the crystallographic phases identified for those particles are respectively the γ' precipitates, carbonitrides, and monoclinic (m) zirconia (ZrO_2). The latter is known to be the stable crystallographic form of zirconia below 1170 °C [28], which indicates that it can form during both solutionizing at 1080 °C

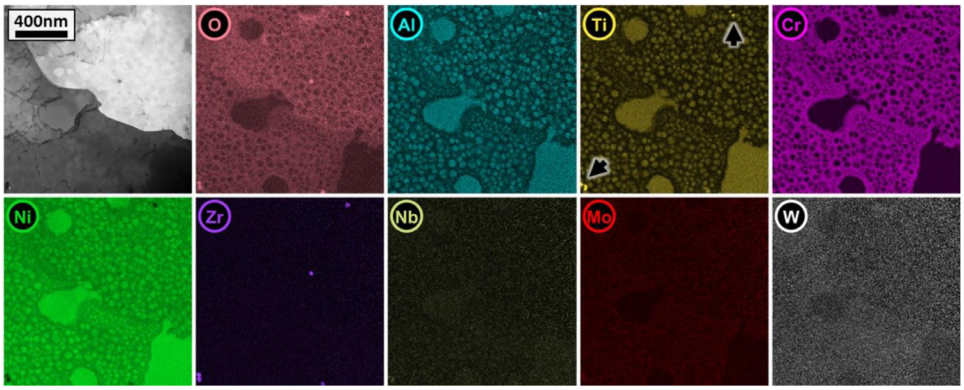

Fig. 3. STEM annular dark-field image and X-ray count maps measured by EDX on a thin foil of the heat-treated microstructure. The colour contrast is proportional to the number of X-rays counted for each element. The annular dark-field image in the top-left corner has been applied a background removal to reduce the contrast induced by differences in the foil thickness.

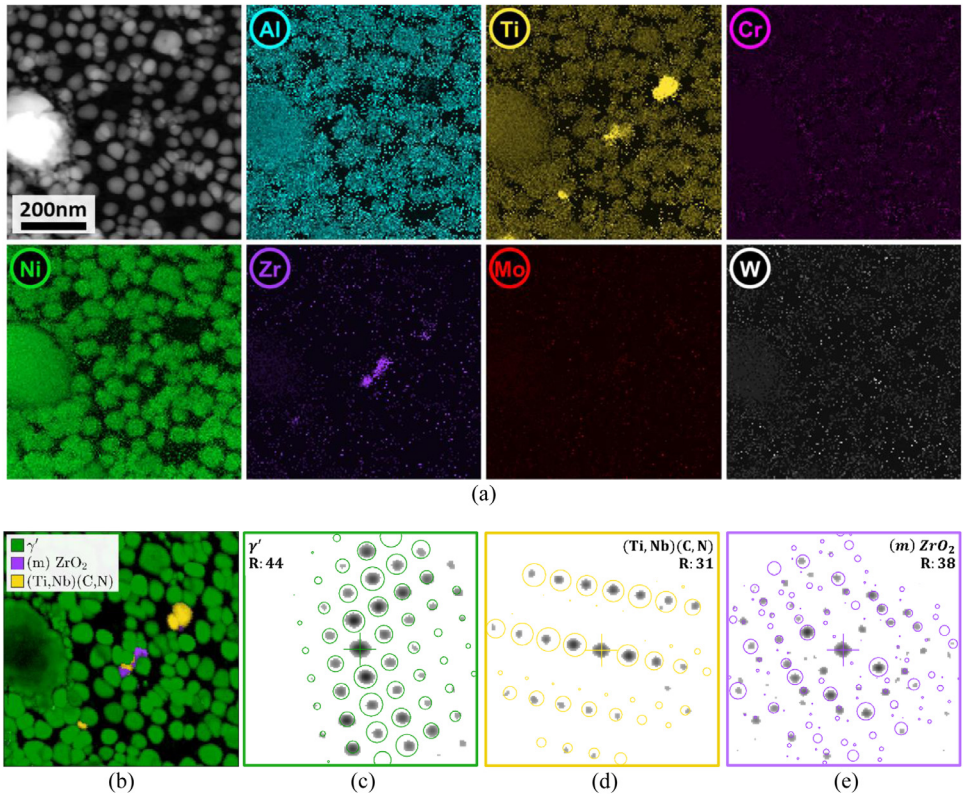

Fig. 4. Observations of a carbon replica prepared from the heat-treated microstructure. (a) STEM annular dark-field image and X-ray count maps measured by EDX. The colour contrast is proportional to the number of X-rays counted for each element. (b) crystallographic phase map obtained by ACOM on the same region of interest. (c-e) examples of acquired diffraction patterns (spots) with the corresponding simulated diffraction patterns (circles).

and ageing at 760 °C. Fig. 4c to e show that the diffraction patterns of the three phases are well indexed. Again, there is a good correspondence between the measured chemistry of the particles and the chemistry expected from the crystallographic phases.

3.2. Elemental partitioning of zirconium

Fig. 5a shows an APT reconstruction of a 41° misorientation angle HAGB prepared from the as-built microstructure. The grain boundary is shown using an isocomposition surface with 1.5 at.% of boron, as done in previous works [2,15]. While Fig. 1 shows no massive presence of γ' precipitates in the as-built microstructure, Fig. 5b shows nano-sized γ' precipitates near the grain boundary, which confirms recent observations [15,25,27]. The difficulty to image these precipitates by TEM has been discussed in refs. [15,27]. As explained in a previous work [15], the nano-sized γ' precipitates are thought to form in the solid state by cellular precipitation occurring during fabrication. In the very short time during which temperature is sufficiently high to allow grain boundary migration, nano-sized γ' precipitates form behind the moving boundary. The size of the particles corresponds approximately to the boundary migration length.

Fig. 5c shows a 1D composition profile from a cylindrical region of interest (ROI) across the grain boundary. Its location in the reconstruction is shown by arrow #1 in Fig. 5a. In agreement with previous findings [2,5,15], the grain boundary exhibits a strong zirconium segregation, the maximum concentration reaching more than 0.5 at.%. Boron and carbon segregation is also observed.

Fig. 6a shows an APT reconstruction of a 45° misorientation angle HAGB prepared from the heat-treated microstructure. An isocomposition surface of 1.0 at.% boron is used to visualize the grain boundary. Thanks to the 7.0 at.% surface of chromium, the secondary γ' precipitates that formed during heat-treatment are also shown. A 1D composition profile from a cylindrical ROI across the grain boundary is given in Fig. 6c. An increased segregation of boron and carbon is observed, while zirconium has nearly disappeared from grain boundaries. This is an interesting observation, as textbooks often report, on the contrary, that zirconium further segregates at grain boundaries during heat-treatment (where it supposedly improves the creep resistance of superalloys) [7,8].

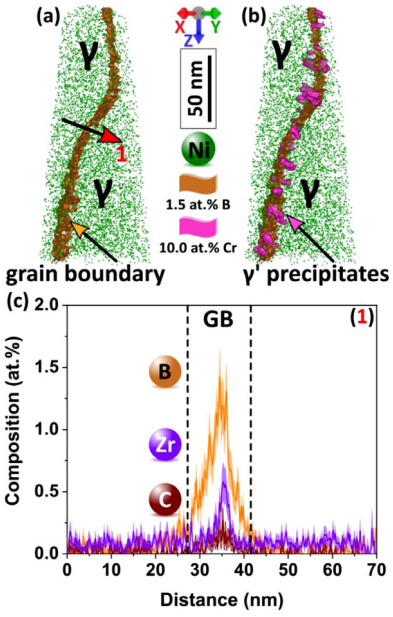

Fig. 5. (a) APT reconstruction of a specimen extracted from the as-built microstructure. The grain boundary coincides with the boron isocomposition surface. (b) the same reconstruction with γ' shown by chromium isocomposition surfaces. (c) 1D composition profile of zirconium across the grain boundary denoted by arrow #1 in (a). The line thickness in (c) corresponds to the 2σ counting error bars.

From the reconstruction shown in Fig. 6b, it appears that zirconium partitions preferentially in γ' precipitates. This is confirmed by the proximity histogram in Fig. 6d, taken at a γ/γ' interface, and showing a higher concentration of zirconium in the γ' precipitates than in the γ matrix.

3.3. Formation of zirconia

Several observations suggest that zirconia does not form during heat-treatment by a classical nucleation and growth of a new phase from the matrix, but by reduction of the alumina particles during heat-treatment. First, alumina particles are only found in the as-built microstructure, while zirconia only in the heat-treated microstructure. Secondly, carbonitrides are often found attached to both types of particles. The solvus temperature of carbonitrides is estimated by a number of authors to be above 1300 °C [12,29,30], while that of alumina is around 2050 °C, and that of zirconia is near 2700 °C [31]. None of these particles can dissolve during heat-treatment at 1080 °C nor, of course, at 760 °C. Thus, the fact that carbonitrides are appended to both types of oxides indicates that the same particles are either alumina in the as-built microstructure, or zirconia in the heat-treated microstructure.

On Ellingham diagrams [32,33], above approximately 700 °C, the Gibbs energy of zirconia formation ($Zr + 0_2 \rightarrow ZrO_2$) is lower than that required for alumina formation ($\frac{4}{3}Al + O_2 \rightarrow \frac{2}{3}Al_2O_3$). As a result, during the applied heat-treatment, zirconium is expected to reduce alumina following the reaction: $Zr + \frac{2}{3}Al_2O_3 \rightarrow ZrO_2 + \frac{4}{3}Al$. Using the Thermo-calc 2019a software with the TCOX database, the Gibbs energy of the reduction of alumina by zirconium is estimated to −14 kJ per mole of oxygen at 1080 °C, and −3 kJ per mole of dioxygen at 760 °C in agreement with the Ellingham diagrams. Fig. 7 summarizes schematically the transformation of alumina in zirconia during heat-treatment.

Now considering that zirconia is thermodynamically more stable than alumina, one may be surprised that alumina has formed prior to zirconia. As it mentioned earlier, the presence of nano-sized alumina particles is often reported in the as-built microstructure of nickel-based superalloys [4,11,26,34], but never zirconia. The early formation of alumina compared to zirconia cannot be attributed either to the differences

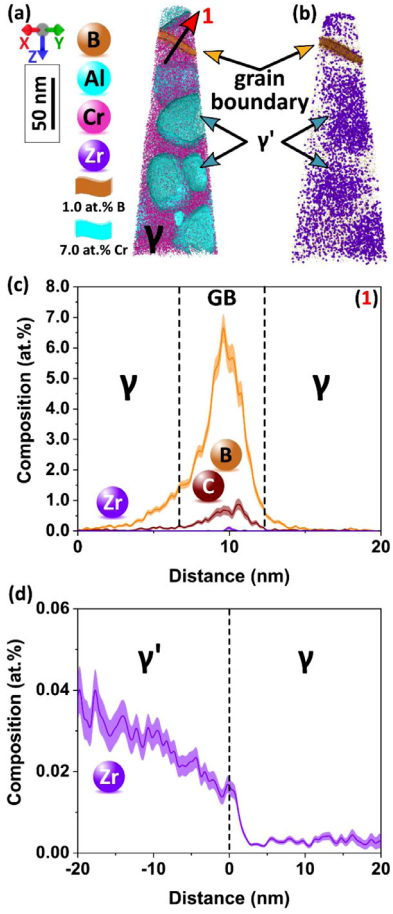

Fig. 6. (a) APT reconstruction of a specimen extracted from the heat-treated microstructure. The grain boundary coincides with the boron isocomposition surface. (b) APT reconstruction showing the Zr-distribution. (c) 1D composition profile across the grain boundary as denoted by arrow #1 shown in (a). (d) Proximity histogram of zirconium across all γ/γ' interfaces in this reconstruction, for precipitates located away from the grain boundary. The line thickness in (b) and (c) corresponds to the 2σ counting error bars.
Discussion.

in the diffusivity of those two elements, since zirconium is known to be a 'fast diffuser' in the nickel matrix [35]. By elimination, we believe that the presence of alumina particles in the as-built state can only be explained by the fact that aluminium is present in a much larger fraction than zirconium in the nominal composition of the alloy (5.07 at.% for aluminium vs. 0.028 at.% for zirconium) and it is therefore more readily available for combining with oxygen during powder atomization and fabrication.

It can be noticed that in several works on superalloys fabricated by powder metallurgy, with similar oxygen levels as for additive manufacture, zirconia has also been detected in the microstructure [36,37]. By contrast, in cast and wrought alloys, where the oxygen content is negligible, zirconium was found to have a high affinity for carbides [9]. Thus, the state-of-the-art support the idea that the trapping of zirconium by oxides is specific to alloys fabricated by powder based processes. In the case where there are no oxides in the microstructure, zirconium is still expected to partition to precipitates during heat-treatment, namely carbides.

3.4. Partitioning of zirconium in the heat-treated microstructure

The results presented above suggest that, in the heat-treated microstructure, zirconium is almost exclusively found in γ' precipitates and in oxides. The amount of zirconium trapped in oxides in the heat-treated

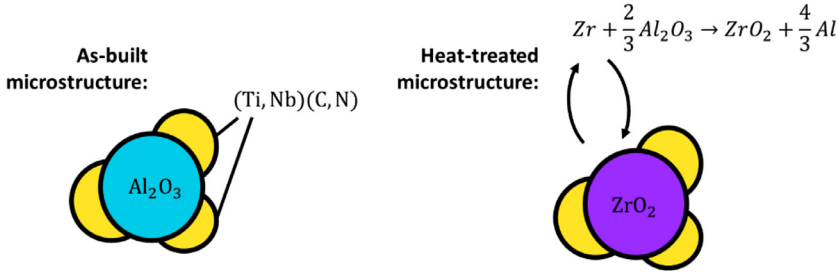

Fig. 7. Schematic of the reduction of alumina (present in the as-built microstructure) by zirconium during heat-treatment, causing the formation of zirconia.

Table 3
Atomic balance of Zr in the heat-treated microstructure.

	γ'	γ	ZrO_2	Total
Zr content in the phase (at.%)	0.03%	0.004%	33.3%	
Phase fraction (at.%)	34%	66%	0.0525%	
Amount of zirconium trapped in the phase (at.%)	0.010%	0.0026%	0.017%	0.029%

microstructure can be estimated assuming that all the oxygen found in parts after fabrication (0.0350 at.%) goes into Zr-rich oxides, and that oxides do not dissolve during heat-treatment. This assumption is reasonable according to the recent work of Haines et al. [14], who have shown in a ferritic stainless steel fabricated by L-PBF, under various atmospheres that the amount of oxygen estimated from the volume fraction of oxides matches closely the amount estimated from macroscopic chemical analysis. It seems reasonable to extend this result to nickel-based superalloys, since the solubility of oxygen in the iron-matrix of stainless steels is of the same order of magnitude as for the nickel-matrix of superalloys. The amount of zirconium trapped in oxides, for one mole of material, can be estimated by $[Zr]_{oxides} = f_{ZrO_2} \times [Zr]_{ZrO_2}$, with f_{ZrO_2} the molar fraction of oxides per mole of material, and $[Zr]_{ZrO_2}$ the molar fraction of zirconium per mole of oxide. To find the zirconia molar fraction, we assume that oxygen limits the oxide fraction. Thus, the nominal fraction of oxygen in the material is related to the fraction of zirconia by $[O]_{nominal} = f_{ZrO_2}[O]_{ZrO_2}$, with $[O]_{ZrO_2} = 66,6\%$ the molar fraction of oxygen in zirconia (since there needs 2 atoms of oxygen and 1 atom of zirconium to form zirconia). By rearranging this relation, we get $f_{ZrO_2} = (\frac{3}{2}) \times 0.035 = 0.0525$ at.%. In addition, $[Zr]_{ZrO_2} = 33.3$ at.%. This amounts to f_{ZrO_2} =0.0173 at.% of zirconium trapped in oxides per mole of material, which makes nearly 60% of the nominal composition of the alloy in zirconium. This must be considered as an upper bound estimate, as it is based on a conservative assumption regarding the composition and fraction of oxides.

In Fig. 6d, the average content of zirconium in γ' precipitates and the γ matrix is roughly 0.03 at.% and 0.004 at.%, respectively. Using equilibrium simulations performed with the TCNI9 and the Thermocalc 2019a software, we estimate that, for this alloy, the fraction of γ' precipitates is 34 at.% at the end of the heat-treatment (at 700 °C), and that of γ phase is 66 at.%. It is reasonable to consider these estimates as accurate, since the AD730 alloy has been the subject of several thorough comparison to Thermocalc predictions [38,39]. The amount of zirconium trapped in the γ matrix and γ' precipitates can then be calculated using similar principles as for the oxides (see Table 3).

The estimated total amount of zirconium trapped in the different constituents of the microstructure – γ, γ' and oxides – is 0.029 at.%, while the nominal composition is 0.028 at.% (Table 1). The excellent agreement between the estimate and the nominal composition further supports the idea that in the heat-treated microstructure, zirconium is trapped away from grain boundaries. This is in clear contradiction with the usual statement in textbooks [7,8]. Since zirconium does not segregate at grain boundaries in the heat-treated microstructure, it also strongly questions its alleged role on the creep resistance.

Another potential benefit of removing zirconium would be to reduce the hot-cracking sensitivity during fabrication. Based on the present observations, one could probably remove zirconium from the nominal composition without loss of creep resistance. This would be consistent with a recent studies having evaluated the creep resistance of alloys without zirconium fabricated by additive manufacturing [6,15]. From a microstructural point of view, if zirconium was to be removed from the nominal composition, oxides would still exist under the form of alumina, and the fraction of γ' would likely remain unchanged (given the small solubility of zirconium in this phase). In addition, the content of zirconium in γ' and γ is likely too small to have a significant effect on the mechanical properties of these phases.

4. Conclusion

We revealed the true partitioning character of zirconium in the as-built and heat-treated microstructures of a nickel-based superalloy processed by L-PBF fusion. In the as-built microstructure, zirconium is almost exclusively located at grain boundaries. During heat-treatment, zirconium migrates away from grain boundaries and reduces alumina nano-particles to form zirconia. A significant fraction of zirconium also partitions in γ' precipitates, and, to a lesser extent, in the γ matrix. This leads to a nearly complete trapping of zirconium away from grain boundaries. This result contradicts several classic textbooks on the topic asserting that zirconium segregates at grain boundaries after heat-treatment.

If zirconium was to be removed from the nominal composition of the superalloy, nano-oxides would still exist in the form of alumina, the fraction of γ' precipitates would remain unchanged, and more importantly the hot cracking sensitivity during fabrication would decrease. These results should be applicable to a large spectrum of polycrystalline superalloys processed by additive manufacturing, since zirconium and oxygen have in general a very low solubility in the nickel matrix.

Declaration of Competing Interest

The authors declare that they have no known competing financial interests or personal relationships that could have appeared to influence the work reported in this paper.

Acknowledgements

This work was financially supported by Aubert & Duval as part of the SOFIA project (BPI France) and has benefited from the equipment of the Grenoble INP - CMTC platform supported by the Centre of Excellence of Multifunctional Architectured Materials "CEMAM" n°ANR-10-LABX-44–01. S.A. would like to acknowledge financial support from the Alexander

Humbolt foundation. Uwe Tezins and Andreas Sturm are acknowledged for their support to the FIB & APT facilities at MPIE.

Supplementary materials

Supplementary material associated with this article can be found, in the online version, at doi:10.1016/j.addlet.2021.100011.

References

[1] M. Cloots, P.J. Uggowitzer, K. Wegener, Investigations on the microstructure and crack formation of IN738LC samples processed by selective laser melting using Gaussian and doughnut profiles, Mater. Des. 89 (2016) 770–784, doi:10.1016/j.matdes.2015.10.027.

[2] A. Hariharan, L. Lu, J. Risse, A. Kostka, B. Gault, E.A. Jägle, D. Raabe, Misorientation-dependent solute enrichment at interfaces and its contribution to defect formation mechanisms during laser additive manufacturing of superalloys, Phys. Rev. Mater. 3 (2019) 123602, doi:10.1103/PhysRevMaterials.3.123602.

[3] D. Grange, J.D. Bartout, B. Macquaire, C. Colin, Processing a non-weldable nickel-base superalloy by Selective Laser Melting: role of the shape and size of the melt pools on solidification cracking, Materialia 12 (2020) 100686, doi:10.1016/j.mtla.2020.100686.

[4] A. Després, C. Mayer, M. Veron, E.F. Rauch, M. Bugnet, J.J. Blandin, G. Renou, C. Tassin, P. Donnadieu, G. Martin, On the variety and formation sequence of second-phase particles in nickel-based superalloys fabricated by laser powder bed fusion, Materialia 15 (2021) 101037, doi:10.1016/j.mtla.2021.101037.

[5] R. Engeli, T. Etter, S. Hövel, K. Wegener, Processability of different IN738LC powder batches by selective laser melting, J. Mater. Process. Technol. 229 (2016) 484–491, doi:10.1016/j.jmatprotec.2015.09.046.

[6] Y.T. Tang, C. Panwisawas, J.N. Ghoussoub, Y. Gong, J.W.G. Clark, A.A.N. Németh, D.G. McCartney, R.C. Reed, Alloys-by-design: application to new superalloys for additive manufacturing, Acta Mater. 202 (2021) 417–436, doi:10.1016/j.actamat.2020.09.023.

[7] R.C. Reed, The Superalloys: Fundamentals and Applications, Cambridge University Press, Cambridge, 2006, doi:10.1017/CBO9780511541285.

[8] M.J. Donachie, S.J. Donachie, Superalloys: a Technical guide, 2. ed., 3. print, ASM, Materials Park, Ohio, 2008.

[9] Y. Murata, N. Yukawa, Solid-state reaction for ZrC formation in a Zr-doped nickel-based superalloy, Scr. Metall. 20 (1986) 693–696.

[10] H. Gruber, M. Henriksson, E. Hryha, L. Nyborg, Effect of powder recycling in electron beam melting on the surface chemistry of alloy 718 powder, Metall. Mater. Trans. A. 50 (2019) 4410–4422, doi:10.1007/s11661-019-05333-7.

[11] H. Yu, S. Hayashi, K. Kakehi, Y.L. Kuo, Study of formed oxides in IN718 alloy during the fabrication by selective laser melting and electron beam melting, Metals (Basel) 9 (2019) 19, doi:10.3390/met9010019.

[12] A. Mitchell, S.L. Cockcroft, C.E. Schvezov, A.J. Schmalz, J.N. Loquet, J. Fernihough, Primary carbide and nitride precipitation in superalloys containing niobium, High Temp. Mater. Process. 15 (1996) 27–40, doi:10.1515/HTMP.1996.15.1-2.27.

[13] K. Harris, J.B. Wahl, Developments in superalloy castability and new applications for advanced superalloys, Mater. Sci. Technol. 25 (2009) 147–153, doi:10.1179/174328408X355442.

[14] M.P. Haines, N.J. Peter, S.S. Babu, E.A. Jägle, In-situ synthesis of oxides by reactive process atmospheres during L-PBF of stainless steel, Addit. Manuf. 33 (2020) 101178, doi:10.1016/j.addma.2020.101178.

[15] A. Després, S. Antonov, C. Mayer, C. Tassin, M. Veron, J.J. Blandin, P. Kontis, G. Martin, On the role of boron, carbon and zirconium on hot cracking and creep resistance of an additively manufactured polycrystalline superalloy, Materialia 19 (2021) 101193, doi:10.1016/j.mtla.2021.101193.

[16] E.F. Rauch, M. Véron, Automated crystal orientation and phase mapping in TEM, Mater. Charact. 98 (2014) 1–9, doi:10.1016/j.matchar.2014.08.010.

[17] O.A. Ojo, N.L. Richards, M.C. Chaturvedi, Microstructural study of weld fusion zone of TIG welded IN 738LC nickel-based superalloy, Scr. Mater. 51 (2004) 683–688, doi:10.1016/j.scriptamat.2004.06.013.

[18] S.M. Seo, I.S. Kim, J.H. Lee, C.Y. Jo, H. Miyahara, K. Ogi, Eta Phase and boride formation in directionally solidified Ni-base superalloy IN792 + Hf, Metall. Mater. Trans. A. 38 (2007) 883–893, doi:10.1007/s11661-007-9090-0.

[19] E. Husson, Y. Repelin, Structural studies of transition aluminas. Theta alumina, Eur. J. Solid State Inorg. Chem. 33 (1996) 1223–1231.

[20] Y. Repelin, E. Husson, Etudes structurales d'alumines de transition. I-alumines gamma et delta, Mater. Res. Bull. 25 (1990) 611–621, doi:10.1016/0025-5408(90)90027-Y.

[21] R.W.G. Wyckoff, Crystal Structures, 2nd ed., Interscience Publishers, New York, 1963.

[22] G. Katz, X-Ray diffraction powder pattern of metastable cubic ZrO_2, J. Am. Ceram. Soc. 54 (1971) 531 –531, doi:10.1111/j.1151-2916.1971.tb12197.x.

[23] C.J. Howard, R.J. Hill, B.E. Reichert, Structures of ZrO_2 polymorphs at room temperature by high-resolution neutron powder diffraction, Acta Crystallogr. B. 44 (1988) 116–120, doi:10.1107/S0108768187010279.

[24] K. Thompson, D. Lawrence, D.J. Larson, J.D. Olson, T.F. Kelly, B. Gorman, In situ site-specific specimen preparation for atom probe tomography, Ultramicroscopy 107 (2007) 131–139, doi:10.1016/j.ultramic.2006.06.008.

[25] X. Wang, L.N. Carter, B. Pang, M.M. Attallah, M.H. Loretto, Microstructure and yield strength of SLM-fabricated CM247LC Ni-Superalloy, Acta Mater. 128 (2017) 87–95, doi:10.1016/j.actamat.2017.02.007.

[26] A. De Luca, C. Kenel, S. Griffiths, S.S. Joglekar, C. Leinenbach, D.C. Dunand, Microstructure and defects in a Ni-Cr-Al-Ti γ/γ' model superalloy processed by laser powder bed fusion, Mater. Des. 201 (2021) 109531, doi:10.1016/j.matdes.2021.109531.

[27] S. Griffiths, H. Ghasemi Tabasi, T. Ivas, X. Maeder, A. De Luca, K. Zweiacker, R. Wróbel, J. Jhabvala, R.E. Logé, C. Leinenbach, Combining alloy and process modification for micro-crack mitigation in an additively manufactured Ni-base superalloy, Addit. Manuf. 36 (2020) 101443, doi:10.1016/j.addma.2020.101443.

[28] S. Block, J.A.H.D. Jornada, G.J. Piermarini, Pressure-temperature phase diagram of zirconia, J. Am. Ceram. Soc. 68 (1985) 497–499, doi:10.1111/j.1151-2916.1985.tb15817.x.

[29] A. Formenti, A. Eliasson, A. Mitchell, H. Fredriksson, Solidification sequence and carbide precipitation in Ni-base superalloys In718, In625 and In939, High Temp. Mater. Process. 24 (2005) 239–258, doi:10.1515/HTMP.2005.24.4.239.

[30] J. Zhang, R.F. Singer, Effect of Zr and B on castability of Ni-based superalloy IN792, Metall. Mater. Trans. A. 35 (2004) 1337–1342, doi:10.1007/s11661-004-0308-0.

[31] M. Yoshimura, Phase stability of zirconia, Am. Ceram. Soc. Bull. 67 (1988) 1950–1955.

[32] T.B. Reed, J. Klerer, Free energy of formation of binary compounds: an atlas of charts for high-temperature chemical calculations, J. Electrochem. Soc. 119 (1972) 329Ca, doi:10.1149/1.2404111.

[33] R.L. Miller, G.A. Reimann, Thermodynamics of gas-metal-slag equilibria for applications *in situ* and *ex situ* vitrification melts, 1993. 10.2172/10170082.

[34] Y.L. Kuo, K. Kakehi, Influence of powder surface contamination in the Ni-based superalloy alloy718 fabricated by selective laser melting and hot isostatic pressing, Metals (Basel) 7 (2017) 367, doi:10.3390/met7090367.

[35] C.Z. Hargather, S.L. Shang, Z.K. Liu, Data set for diffusion coefficients and relative creep rate ratios of 26 dilute Ni-X alloy systems from first-principles calculations, Data Brief 20 (2018) 1537–1551, doi:10.1016/j.dib.2018.08.144.

[36] L. Tan, G. He, F. Liu, Y. Li, L. Jiang, Effects of temperature and pressure of hot isostatic pressing on the grain structure of powder metallurgy superalloy, Materials 11 (2018) 328, doi:10.3390/ma11020328.

[37] J.S. Crompton, R.W. Hertzberg, Analysis of second phase particles in a powder metallurgy HIP nickel-base superalloy, J. Mater Sci. 21 (1986) 3445–3454, doi:10.1007/BF02402986.

[38] F. Masoumi, D. Shahriari, M. Jahazi, J. Cormier, A. Devaux, Kinetics and Mechanisms of γ' Reprecipitation in a Ni-based Superalloy, Sci. Rep. 6 (2016) 1–16, doi:10.1038/srep28650.

[39] A. Devaux, A. Helstroffer, J. Cormier, P. Villechaise, J. Douin, M. Hantcherli, F. Pettinari-Sturmel, in: Effect of Aging Heat-Treatment On Mechanical Properties of AD730TM Superalloy, in: 8th Int. Symp. Superalloy 718 Deriv, John Wiley & Sons, Ltd, 2014, pp. 521–535, doi:10.1002/9781119016854.ch41.